Piezoelectric Elliptical Plate Micromechanical Resonator with Low Motional Resistance for Resonant Sensing in Liquid

Habiba Begum, Jingui Qian, and Joshua E.-Y. Lee, *Senior Member, IEEE*

***Abstract*— Key to realizing practical resonators for liquid-phase sensing applications is efficient electromechanical transduction and reasonable *Q* in liquid, which determine the motional resistance (R_m). Both lower R_m and high liquid phase *Q* are important for realizing a more stable close-loop oscillator to allow a lower detection limit. But R_m usually increases when scaling down resonator size, leading to weak output signals in liquid. This paper describes a piezoelectrically transduced micromechanical elliptical plate resonator (EPR) targeting liquid-phase sensing applications. The proposed EPR delivers lower R_m relative to other disk-based modes and has a reasonable *Q* in water. These two features are critical for eventually realizing a closed-loop system to enable real-time frequency tracking for sensing applications. The low R_m arises from enhanced transduction efficiency associated with the modal lateral strain profile. The EPR's moderate liquid phase *Q* stems from transducing a stiff lateral bulk mode that increases energy storage. The proposed EPR can be scaled down more efficiently compared to other disk-based modes in the limit of mode shape distortion by anchors when scaling down the resonator below a threshold. Experimental results in water are demonstrated for a 500 µm by 400 µm EPR, which delivers an R_m of only 2.68 kΩ in water without feedthrough cancellation. Scaling down the device to 300 µm by 200 µm, we demonstrate an R_m of just 5.5 kΩ and *Q* of 245 in water. The proposed EPR topology boasts the lowest R_m among resonators immersed in liquid after normalizing over the device area.**

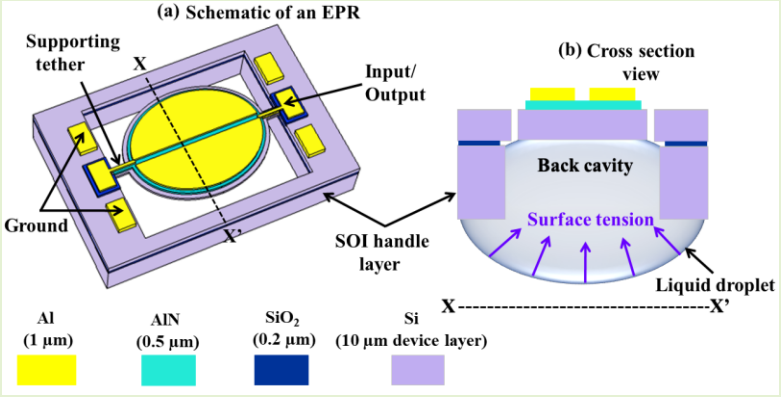

***Index Terms*— Disk resonators, liquid-phase sensing, MEMS resonators, piezoelectric devices, quality factor.**

I. Introduction

MICROMECHANICAL resonant devices have been of interest for gravimetric sensing applications. Miniaturization of these devices allows for higher mass sensitivity [1-3]. As such, micromechanical resonators are an attractive alternative to conventional sensors such as QCMs. Micromechanical resonant devices have progressed to now target liquid phase sensing. Applications of liquid phase sensing using micromechanical resonators include monitoring a wide range of phenomena or interactions (e.g. antigen-antibody binding and DNA-hybridization) as well as a range of fluid substances and parameters (e.g. water quality, blood glucose, and food quality) [4-8]. One key challenge to operating micromechanical resonators in liquid compared to in air is the increased fluidic damping on the resonator, which inevitably reduces the quality factor (*Q*). One well-known approach to reduce dissipation in a fluid is to contain the fluid in the resonator instead of immersing the resonator in the fluid in the form a suspended microchannel resonator (SMRs) [9]. While SMRs can deliver much higher *Q*s as the external interaction between the device and environment is with air molecules rather than liquid, the drawback of SMRs lies in the underlying fabrication process that is much more complex and costly. Optical detection can provide the resolution to pick-up minute vibration amplitudes but are difficult to scale up to increase throughput, thus favoring an electrical readout solution [10].

In the case of realizing electrically addressed resonators, the choice of transduction method is critical given that the

Manuscript received October 09, 2020; revised November 28, 2020, and December 23, 2020; accepted XXX, XX, 20XX. This work was supported by a grant from the Research Grants Council of Hong Kong, University Grants Committee under project number CityU 11218118.

H. Begum and J. Qian are with the department of Electrical Engineering, City University of Hong Kong, Kowloon, Hong Kong. (e-mail: hbegum2-c@my.cityu.edu.hk; jinguqian2-c@my.cityu.edu.hk).

J. E.-Y. Lee is with the department of Electrical Engineering and State Key Lab of Terahertz and Millimeter Waves, City University of Hong Kong, Kowloon, Hong Kong. (e-mail: josh.lee@cityu.edu.hk).

Digital Object Identifier XXXXX

expected output signals are typically weak especially given the low Qs when a resonator operates in liquid. Fig. 1 shows a typical equivalent circuit diagram adapted to represent the electrical behavior of a resonator. The resonant elements (R_m, C_m, L_m) are lumped parameters that model the electromechanical "motional" aspects of the resonators. R_m is the motional resistance that represents the electromechanical losses from the resonator and is inversely proportional on Q. C_m is the motional capacitance and captures the stiffness of the resonator. L_m is the motional inductance and captures the mass of the resonator. The elements in the parallel branch (C_f, R_f) model parasitic sources in relation to the fluidic environment and the device. In the absence of parasitics for simplicity of illustration, the motional resistance (R_m) defines the admittance at the resonant frequency, ω_0 (i.e. peak value). By definition,

$$\frac{1}{R_m} = \omega_0 C_m Q \tag{1}$$

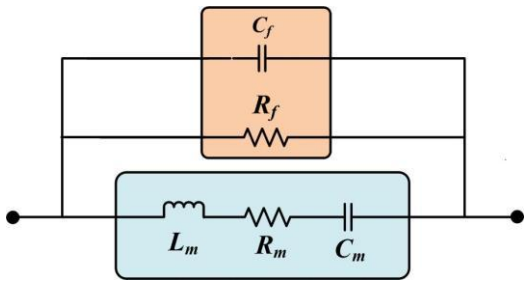

Fig. 1. Electrical equivalent circuit model of a resonator.

For liquid-phase applications, piezoelectric transduction has been gaining more traction more recently compared to more conventional transduction methods like capacitive and thermal-piezoresistive as piezoelectric transduction offers more efficient electromechanical coupling [11]. As an illustration, by simply changing the method of transduction in same rotational mode disk resonator from thermal-piezoresistive transduction to piezoelectric transduction, the motional resistance (R_m) was reduced from 10.64 kΩ [12] to 5.6 kΩ [13]. It is worth noting that the observed drop in R_m comes despite a decrease in Q, which implies an increase in motional capacitance (C_m) according to equation (1) given that the resonant frequencies are similar in [12] and [13] for the same resonant mode. As C_m is proportional to the square of the transduction factor, we thus see that the change in transduction method from thermal-piezoresistive to piezoelectric affords an increase in transduction factor in the case of the rotational mode. Besides flexural modes [14], various in-plane bulk modes have been explored in relation to their effect on Q, including quadrilateral plates [15-16] and disks [17-18]. Disk-based modes have been rather popular, as they have been shown to be capable of delivering higher Qs in liquid through innovative design and transduction of various vibration modes [12-13, 17-25]. The rotational mode disk resonator reported in [12] is an excellent example of realizing high Q in liquid. However anchoring these disk resonators can be a challenge [20], especially in the context of downscaling the device area to increase mass sensitivity in the limit of a finite minimum anchor width that can be fabricated reliably. Scaling down the device area below a certain limit could result in the anchors distorting the mode shape and adversely affect the transduction efficiency. One recent approach aimed at addressing anchoring restrictions has been to exploit the elastic anisotropy in single-crystal silicon while exciting higher-order modes in a disk resonator; a design that delivers possibly the highest Qs in liquid [20]. The disk was anchored with thin and short beam tethers and to reduce acoustic radiation to substrate, in-plane reflectors were etched near the anchors. As in the case of all higher order modes, the associated acoustic wavelength is much shorter than the diameter of the resonator. As such, more aggressive downscaling of the device to scale up mass sensitivity could be highly challenging in the limit of a minimum tether width that can be realized.

As implied by equation (1), R_m scales inversely with the motional capacitance (C_m) of the resonator. In the case of disk resonators, where most of the vibration modes are defined by strain components in both axes within the plane, C_m scales with the area of the device. For a generic piezoelectric resonator:

$$C_m \propto d_{31}^2 A \tag{2}$$

where d_{31} refers to the piezoelectric coefficient that relates lateral strain fields to vertical electric field, and A is the surface area of the device fully covered with electrodes. If C_0 is defined as the total capacitance of the transducers, then the ratio C_m/C_0 is independent of scaling. As a dimensionless parameter, C_m/C_0 is proportional to certain definitions of the electromechanical coupling coefficient for lateral bulk modes [26]. On the other hand, ω_o scales inversely with the defining feature length (i.e. diameter). In short, assuming Q is independent of lateral scaling for simplicity of illustration, R_m scales inversely with the diameter. Miniaturization inevitably increases R_m. From a broader view, a low R_m is favored for realizing closed-loop systems to enable real-time frequency tracking. In terms of anchoring considerations, clamping the disk along the sides allows access from the rear through a back cavity, which is useful sensing applications. Most of the clamping locations for disk-based modes are quasi-nodes. Downscaling the resonator below a certain threshold will lead to distortion of the vibration mode and associated strain field imposed by the anchors and C_m/C_0 could be significantly reduced. The effect of anchors on strain field distortion is highly dependent on the resonator mode and shape.

In this paper, we propose an alternative resonant mode based on an elliptical plate resonator (EPR) that delivers a reasonable value of Q in water but much lower R_m compared to other disk-based modes fabricated using the same process. The proposed EPR represents a balance between coupling efficiency and ease of clamping to allow more efficient downscaling of the resonator compared to other disk-based modes. Apart from disk-based modes, the EPR topology has also a lower R_m compared to rectangular plate modes of similar size. Overall, the proposed EPR topology represents the lowest R_m among resonators immersed in liquid reported in the literature after normalizing over the device area for fair comparison in the context of mass sensing. In this paper, we demonstrate the EPR based on an Aluminum Nitride on Silicon foundry process [27].

II. Device Description

Fig. 2(a) shows the finite element (FE) simulated displacement profile of the EPR using COMSOL Multiphysics viewed from the top. For a given plate thickness, the EPR structure is defined by two geometrical features: the radius along the major axis (symbolized by r_a) and the radius along the minor axis (symbolized by r_b). In the case of the EPR shown in Fig. 2(a), r_a = 250 µm and r_b = 200 µm. The EPR is clamped along the major axis (i.e. x-axis) where the displacement is notably smaller than in the minor axis. (i.e. y-axis). In the FE simulations, we adapted the anisotropic stiffness matrix of single-crystal silicon. In the actual device, the resonator comprised three layers: single-crystal silicon (10 µm thick), Aluminum Nitride (0.5 µm) and Aluminum (1 µm). In the simulations shown in Fig. 2, only the silicon layer was considered for simplicity of illustration as the other film layers are much thinner and verified to have little effect on the mode shape and resonant frequency. The x-axis of the EPR was aligned along the <100> direction. Fig. 2(b) shows the corresponding strain profile of the vibration mode. The maximum stress is concentrated at the center of the EPR. When the EPR is in expansion, the anchoring beams experience some measure of contraction. As such, the chosen clamping location is a quasi-node given the non-zero strain field in the anchoring beam. Nonetheless, these anchoring beams do not significantly distort the mode shape. As will be seen from the experimental results later, the strain in the anchors that could give rise to anchor loss has minimal impact on the quality factor (Q) of the EPR in a liquid like water.

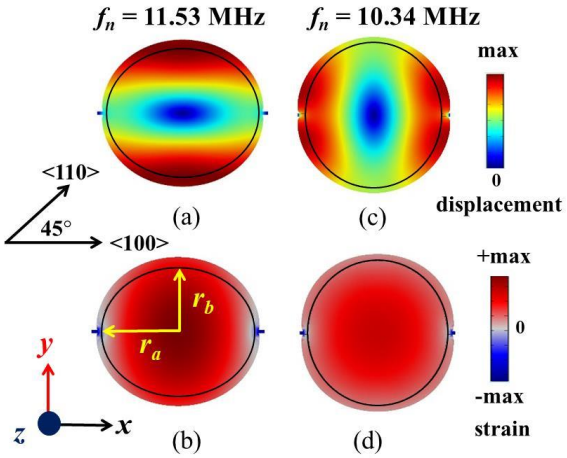

Fig. 2. Vibration mode shape based on the EPR in terms of the (a) total displacement (vector sum) profile and (b) corresponding lateral strain profile ($\varepsilon_x + \varepsilon_y$). For comparison we, simulated the radial contour mode based on a perfect circle disk resonator in terms of the (c) total displacement (vector sum) profile and (d) corresponding lateral strain profile ($\varepsilon_x + \varepsilon_y$). Radius along the clamped axis (r_a) of the EPR and the radius of the perfect circle disk are the same, r_a = 250 µm. Radius along the free axis of the EPR, r_b = 200 µm. Anisotropic properties of silicon were adapted in the FE simulation; x-axis aligned along the <100> direction.

The strain field depicted in Fig. 2(b) represents the sum of in-plane strain components (i.e. $\varepsilon_x + \varepsilon_y$, where ε_x and ε_y respectively denote the strain in the x-axis and y-axis). In the case of piezoelectric transduction, the electrode locations should overlap with the regions of maximum strain. As such, the concentration of the strain field at the center of the EPR as shown in Fig. 2(b) allow convenient placement of transducer electrodes in the design.

For comparison, we show the FE simulated displacement profile of a (perfect circle) disk resonator vibrating in the breathing or radial-contour mode in Fig. 2(c), i.e. when r_b/r_a = 1. Due to the symmetry of the disk in both the x-axis and y-axis, the displacement and strain profiles are theoretically the same. The simulated disk resonator has been clamped along its diameter, likewise in the <100> direction. Comparing the displacement profiles of the EPR (Fig. 2(a)) and the radial-contour mode (Fig. 2(c)), the presence of the anchoring beams result in far more significant distortion of the mode in the radial-contour mode than in the EPR. The difference is due to the asymmetry between displacements in the x-axis (clamped axis) and y-axis (free axis) in the case of the EPR. Given that the anchors have a significant effect on the vibration mode, it is common to adapt a T-shaped tether for side-clamped disk resonators to increase the compliance of the tether as the disk resonator stretches and compresses against the tether [21]. Reducing compliance requires fabricating parts of the tether to narrow, which imposes a practical bottleneck when scaling down a disk resonator. Clamping the disk resonator from the center would eliminate the need for side-clamping, and center anchoring is most commonly done from the bottom using a front side release process [22]. However, clamping the disk resonator from the bottom eliminates access to the resonator through the back cavity, which can be useful for liquid-sensing applications [23]. Alternative modes based on the disk resonator include the widely reported wine glass mode [24] and more complex modes like the button-like mode that can be clamped without using T-shaped tethered. Nonetheless, as shown by its strain profile, the radial-contour mode is highly attractive for piezoelectric transduction, as the strain field concentrated at the center of the disk is comprised of strain components in the x- and y- axes in equal measure. Compared to most other in-plane modes found in a disk resonator, the radial-contour provides the highest coupling efficiency typified by a high C_m value, which in turn helps reduce R_m.

As such, the proposed EPR topology aims to exploit the benefits of a radial-contour mode's strain profile (mutual reinforcement of strain fields from both axes) to provide enhanced transduction efficiency while at the same time easing the clamping requirements to afford a pathway for downscaling in the context of mass sensing. Both these aims are pursued simultaneously by breaking the symmetry present in the radial-contour mode of the perfect circle disk. The result is that the strain and displacement fields along the free axis are larger than those in the clamped axis. In contrast the strain and displacements fields are the same for the perfect circle.

As the symmetry of the radial-contour mode is broken in the EPR, changing r_b while keeping r_a fixed has a notable effect on the resonant frequency as shown in Fig. 3. In Fig. 3, the ratio of the radii between the free and clamped axes (r_b/r_a) is reduced from 0.8 to 0.5 in steps of 0.1 for a fixed radius along the clamped axis (r_a = 250 µm). Although the FE simulated mode shape is defined by strain and displacement components in both lateral axes within the plane, we have confirmed that the resonant frequency is approximately linear with the inverse of r_b within the range of values tested.

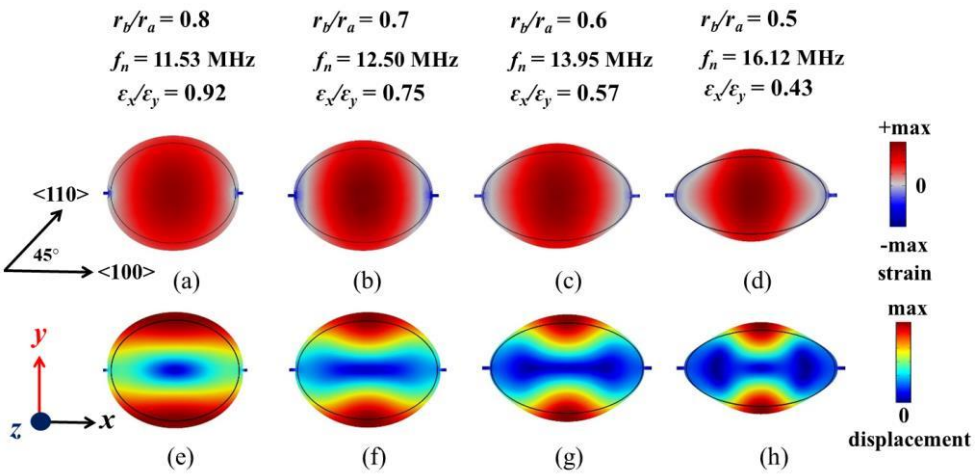

Fig. 3. (a)-(d) Total lateral strain ($\varepsilon_x + \varepsilon_y$) profile of simulated EPRs for different r_b/r_a ratios with the same value of r_a = 250 µm. (e)-(h) corresponding displacement (vector sum) profile of the EPRs as a function of r_b/r_a ratio.

As shown by the simulated mode shapes given in Fig. 3, reducing the r_b/r_a ratio reduces the coverage of tensile strain fields concentrated at the center of the EPR. The anchored regions of the EPR remain in compression even as the r_b/r_a ratio is reduced, rather than non-zero values. In comparing the transduction efficiency in relation to r_b/r_a, we normalized C_m over C_0 given that C_m depends on the transduction area and thus C_0. As such, a comparison in terms of C_m alone provides limited insight when considering the effect of reducing r_b as C_m is expected to decrease according to the reduced area. In the context of mass sensing, basing the comparison upon C_m/C_0 factors in the benefit to mass sensitivity from reducing the device area in relation to r_b. In the FE simulations to compute C_m, the respective EPR models of varying r_b/r_a ratio each have electrode areas that fully cover the surface area of the EPR plates. The respective value of C_0 was calculated manually based on the surface area of the respective EPRs. These theoretical values of C_m/C_0 are later compared against the corresponding values extracted from experiments, showing good corroboration. The respective values of the ratio $\varepsilon_x/\varepsilon_y$ labelled in Fig. 3 have been computed from FE by dividing the integral of the x-axis strain field (ε_x) over the integral of the y-axis strain field (ε_y). In the case of a perfect circle disk, $\varepsilon_x/\varepsilon_y$ equals one. As the ratio of r_b/r_a is reduced, we see that $\varepsilon_x/\varepsilon_y$ drops. This trend in the drop in $\varepsilon_x/\varepsilon_y$ is correlated to modifications of the mode shape with changing r_b/r_a. As r_b/r_a decreases, the displacement amplitude along the free axis (U_y) becomes increasingly dominant over the displacement amplitude along clamped axis (U_x). The maximum strain is proportional to the displacement amplitude along the respective axis. As C_m is related to the surface integral of ($\varepsilon_x + \varepsilon_y$), a reduction in the ratio of $\varepsilon_x/\varepsilon_y$ arising from the modification of the mode shape results in a reduction in C_m.

III. Experimental Results & Discussions

The EPRs described in Section II were all fabricated using a standard AlN on silicon-on-insulator (SOI) foundry process [27]. Fig. 4(a) shows a perspective view schematic of an EPR (r_b/r_a = 0.8) depicting the constituent film layers and Fig. 4(b) reveals a cross-sectional view of the EPR across the indicated line section (XX'). As mentioned briefly in Section II, the EPR comprises three layers: 10 µm silicon (Si) device layer, 0.5 µm Aluminum Nitride (AlN) piezoelectric layer, and 1 µm Aluminum (Al) metal layer (with 20 nm adhesion layer of Chromium (Cr)). The Si device layer has been surface-doped, which we use as the ground plane to the piezoelectric transducer. The AlN was reactively sputtered and patterned by wet etching. We have designed the EPRs to be electrically probed in a two-port configuration, as illustrated in Fig. 4(a) and Fig. 4(b), such that one top electrode serves as an input port and a second top electrode as an output electrode. While it is possible to divide the input/output electrodes across the minor axis, we have designed the input/output electrodes to be divided across the major axis, as depicted in Fig. 4(a). Each of the EPRs are supported from the substrate through 30 µm long and 10 µm wide anchoring beams at the two ends of the EPR along the major axis. In the last stage of the fabrication process, the resonator is released from the bulk handling layer by trench-etching through thickness of the handling wafer by Deep Reactive Ion Etching (DRIE), which creates a back cavity opening on the rear side of the resonator. Fig. 5 depicts the SEMs of the fabricated EPRs.

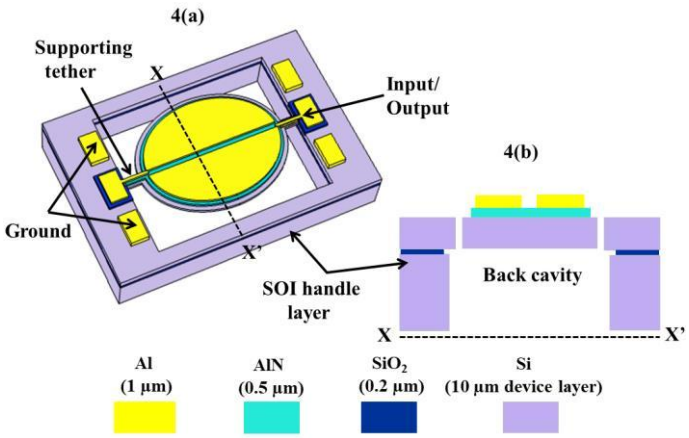

Fig. 4. (a) Perspective view schematic of an EPR (r_b/r_a = 0.8) showing the constituent layers and layout of the top electrodes on the piezoelectric film diagram and (b) cross sectional view of fabricated resonator r_b/r_a = 0.8 demonstrating design details and thickness of each layers. The all other resonators also fabricated following the same process and are unnecessary to describe.

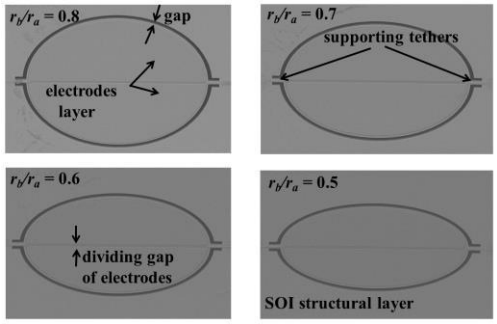

Fig. 5. SEMs of fabricated EPRs. Labels on the top left-corner of each figure specifying the corresponding minor axis (r_b) to major axis (r_a) ratios.

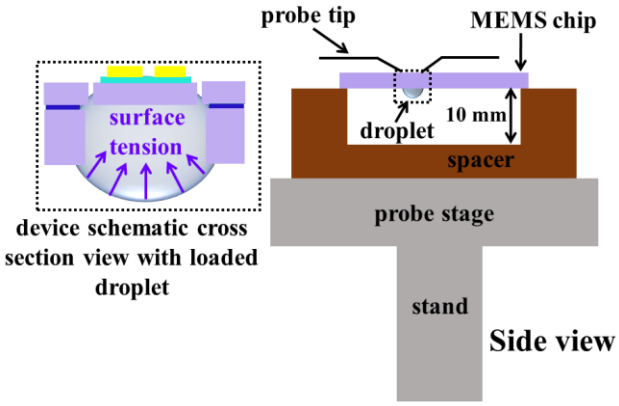

Fig. 6. Schematic of the experimental setup showing the spacer placement and droplet.

A. Electrical Characterization of EPRs

Each of the four EPRs described in Section II were electrically characterized using an Agilent 5061A Network Analyzer using the same input radio frequency (RF) source power of 0 dBm. All the devices were characterized using GSG probes on a probe station. Each device was first measured in air and then with the device immersed in water. For the measurements in water, the back cavity of each device was filled with deionized (DI) water through a pipette by dispensing the same volume of liquid (0.25 µL) in each case with the rear side facing up. This volume of fluid was enough to completely fill the back cavities yet not too small for the pipette to reliably dispense in each experiment.

The schematic of the experimental setup of measurement in liquid is shown in Fig. 6. After filling the back cavity, the fabricated MEMS chip is flipped back so that the top side faces up to probe the resonators from the contact pads on the front side. The liquid droplet in the back cavity of the resonator is held within the walls of the cavity by surface tension forces. To allow room for the droplet surface to extend beyond the height of the cavity, a spacer was placed between the microfabricated chip and sample mounting stage of the probe station. The measured electrical transmission (S_{21}) for each EPR are shown in Fig. 7.

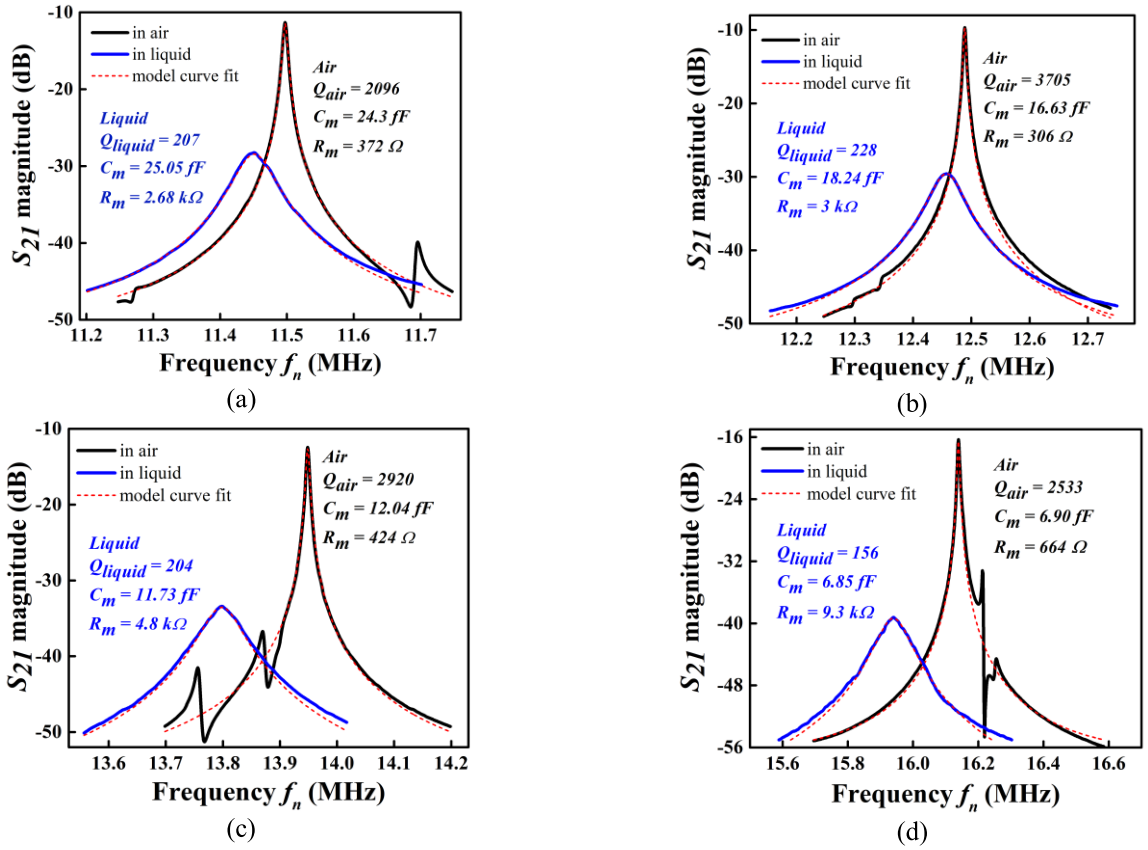

Fig. 7. Measured electrical transmission (S_{21}) for the four EPRs of different r_b/r_a ratios; (a) r_b/r_a = 0.8, (b) r_b/r_a = 0.7, (c) r_b/r_a = 0.6, and (d) r_b/r_a = 0.5. The black solid curves denote the measured S_{21} magnitude in air and the blue solid curves denote the measured S_{21} magnitude in liquid. The red dashed curves represent model-fits based on the equivalent circuit model depicted in Fig. 1. Inset showing the extracted Q-factor, C_m, and R_m of the respective resonators. No de-embedding to remove parasitic feedthrough was required for these measurements.

The equivalent electrical lumped parameters with reference to the circuit model shown previously in Fig. 1 were extracted by fitting the equivalent circuit model to the measured S_{21} of each respective device. Some of the extracted parameters have been included in the respective S_{21} graphs in Fig. 7. The extracted parameters are summarized in Table I. The effects of the parasitic elements, C_f and R_f, on the fitted curve are negligible compared to the strength of the electromechanical signals from each of the EPRs and thus neglected in our curve fits. As such, we have omitted their values in the relevant figures and tables. As seen from Table I, the measured values of resonant frequencies for each EPR agree well with the FE simulations, as is also the case for the values of C_m. As can be seen from Fig. 7, there is a slight downshift in the resonant frequency when each of the EPRs are loaded with DI water due to the loading effect of water on the resonators. The decrease in C_m experimentally as r_b is reduced agrees with the trends predicted by FE simulations as depicted by Fig. 8.

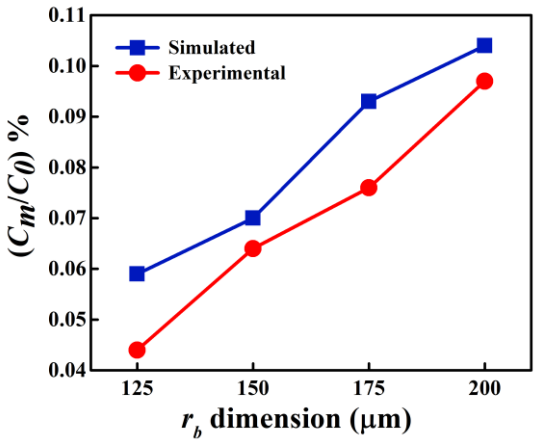

Fig. 8. FE simulated and experimentally derived values or C_m/C_0 as a function of minor axis radius (r_b) for fixed value of major axis radius (r_a = 250 μm).

TABLE I
EXTRACTED LUMPED PARAMETERS OF EPRS IN AIR AND WATER

Parameter	Source	Medium	r_b/r_a = 0.8	r_b/r_a = 0.7	r_b/r_a = 0.6	r_b/r_a = 0.5
f_n (MHz)	Sim.		11.53	12.50	13.95	16.12
	Exp.	air	11.50	12.49	13.95	16.13
		water	11.45	12.46	13.79	15.94
C_m (fF)	Sim.		26.0	20.4	13.2	9.18
	Exp.	air	24.3	16.63	12.04	6.90
		water	25.05	18.24	11.73	6.85
(C_m/C_0)%	Sim.		0.11	0.099	0.075	0.063
	Exp.	air	0.10	0.080	0.067	0.047
		water	**0.105**	0.088	0.067	0.047
Q	Exp.	air	2096	3705	2920	2533
		water	207	**228**	204	156
R_m (kΩ)	Exp.	air	0.372	0.306	0.424	0.664
		water	**2.68**	3	4.8	9.3

Sim. = Simulated result, Exp. = Experimental result.

But even after normalizing C_m over C_0 to account for the reduction in device surface area, C_m/C_0 nonetheless decreases with r_b as depicted by Fig. 8. As such, in reducing r_b/r_a from 0.8 to 0.5, C_m/C_0 decreases. This decrease trend of C_m/C_0 with decreasing r_b/r_a correlates well with the same trend for the aggregate ratio of the strain along the clamped axis over strain along the free axis, as mentioned in Section II. As such, these results indicate that, in terms of transduction efficiency, the optimal r_b/r_a ratio for the EPR is an r_b/r_a ratio closer to unity but less than unity (which is the case of a perfect circle). In terms of Q, the r_b/r_a ratio does not have an obvious effect, at least in the case of operating the resonator in water. Hence, in terms of R_m, it would be desirable for r_b/r_a to be closer to unity (i.e. rounder ellipse). The increase in mass sensitivity gained from a reduction in area by reducing r_b relative r_a is offset to a much greater extent in the drop in C_m as evidenced by the trend of C_m/C_0 in relation to r_b/r_a with little benefit in terms of Q.

B. Comparison Against Disk-Based Modes

Having characterize the EPRs in air and water, we now compare the proposed EPR with vibration modes based on circular disks in terms of Q, R_m and C_m/C_0. We have chosen to compare against disk resonators with a radius equal to major axis radius of the EPR (r_a = 250 μm). The modes for comparison are the radial-contour (RC) mode and button-like (BL) mode. We omit comparisons against the wine glass (WG) mode, which has been described elsewhere as having lower C_m than the BL mode [17]. As such, we have chosen disk-based modes known to yield higher values of C_m and lower R_m (among modes common to disk resonators) for comparison against the proposed EPR. The disk resonator for exciting the RC mode was supported by T-shaped tethers to reduce anchor loss and was probed using a two-port configuration just like the EPR. The BL mode was excited in another disk resonator supported by beam anchors and was probed using a fully differential configuration. Fig. 9 shows the strain profiles, schematics of driving & sensing configuration and the fabricated device SEMs of the RC and BL modes. We applied the same measurement setup used for the EPR (liquid contact from the rear of the device) to the two disk resonators. But when normalized over C_0, thereby accounting for differences in device area, C_m/C_0 for the EPR is slightly higher than the RC mode in the FE simulations.

In the experiments, the extracted value of C_m is notably lower than the value from FE simulations, leading to a further reduction in C_m/C_0 relative to the EPR. The quality factor of the two modes are similar although the EPR has a slightly higher Q than the RC mode. Overall, we see from both the simulations and experiments that the RC mode does not provide a distinct advantage over the EPR in terms of R_m and Q in water, even at these physical dimensions where the T-shaped tethers can be feasibly realized. In designing the T-shaped tethers, we have pushed the foundry fabrication process to its limit. As such, further reduction of the disk resonator cannot be complemented by a scaling of the tethers. In the case of the BL mode, the value of C_m is almost 10% of the EPR as shown in Table II. Despite the resonant frequency of the BL mode being more than double the EPR, the Q in water of the BL mode is not much higher than the EPR. Hence overall, the BL mode exhibits much higher R_m (about four times) compared to the EPR. In summary, compared to disk-based modes, the EPR exhibits lower R_m, which highlights its

attractiveness for liquid-phase mass sensing applications. The results are summarized in Table II. In theory, C_m for the RC mode is higher than an EPR with r_b/r_a = 0.8 due to the lateral strain components in both axes existing in equal measure, as suggested by the FE simulation results in Table II.

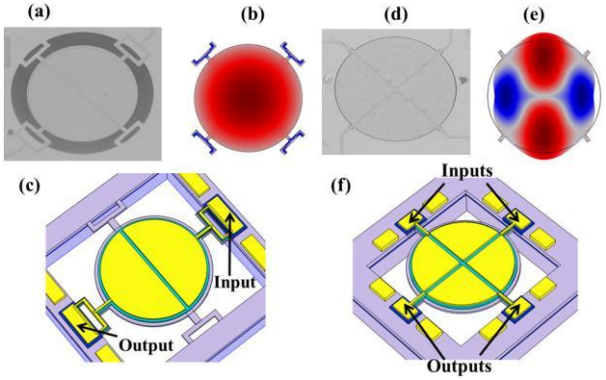

Fig. 9. (a)-(c) showing the SEM, strain profile, and schematic of driving and sensing configuration of radial contour (RC) mode. Similarly (d)-(f) showing the SEM, strain profile, and schematic of driving and sensing configuration of button-like (BL) mode.

TABLE II
COMPARISON OF PERFORMANCE BETWEEN THE EPR AND OTHER DISK-BASED MODES IN WATER

		EPR (r_a = 250 µm, r_b = 200 µm)	RC (r_a = 250 µm)	BL (r_a = 250 µm)
f_n (MHz)	Exp.	11.45	9.87	25.05
Insertion loss (dB)	Exp.	28.9	32.42	41.28
C_m (fF)	Sim.	26	30	2.92
	Exp.	25.05	**28.6**	2.3
Q	Exp.	207	135	**240**
R_m (kΩ)	Exp.	**2.68**	4	11.5
(C_m/C_0) %	Sim.	0.11	0.10	0.0098
	Exp.	**0.105**	0.096	0.0077

C. Experimental Results of Scaled Down EPR

To demonstrate that the EPR can be scaled down without distorting the vibration mode and compromise on C_m/C_0, we designed and fabricated a smaller EPR. The major/clamped axis radius was r_a = 150 µm and the minor/free axis radius was r_b = 100 µm, thus corresponding to an r_b/r_a ratio of 0.67. From FE simulations, scaling the EPR from r_a = 250 µm down to r_a = 150 µm while keeping the r_b/r_a ratio constant at 0.67 (with anchoring beams of the same physical dimensions included in the model), we have verified that C_m/C_0 remains unchanged at around 0.088%. The strain field pattern of the scaled down EPR (shown in Fig. 10(a)) is almost the same as in the case of the EPR with r_a = 250 µm and r_b/r_a = 0.7 (compare with Fig. 3(b)). As such, the EPR can be scaled without resulting in distortion of the mode shape due to the anchors. We applied the same characterization setup (loading of water from the rear of the device) to the scale down EPR. We used a smaller volume of water (0.15 µL) which was enough to fill the back cavity that had been scaled down according to the dimensions of the scaled down EPR. The extracted parameters from measurements are summarized in Table III. Scaling down the size of the device, we see from Table III that the experimental values agree well with those from FE simulations, verifying that reducing the EPR to this scale does not increase the deviation from theory. Compared to the large EPRs with similar r_b/r_a ratios, we have observed that the reduction in C_m is nearly in line with the reduction in device area. Reducing the EPR from r_a = 250 µm by r_b = 175 µm (r_b/r_a = 0.7) to r_a = 150 µm by r_b = 100 µm (r_b/r_a = 0.67), C_m almost scales in proportion with the device surface area.

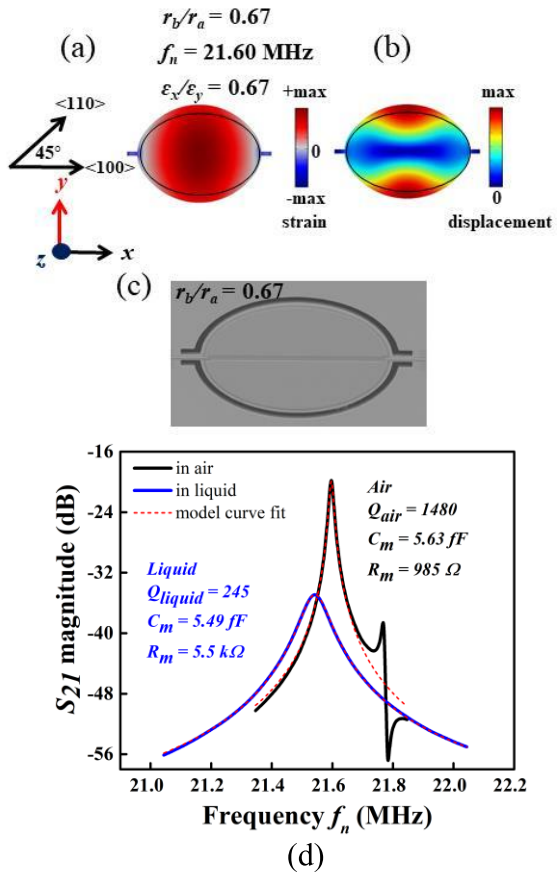

Fig. 10. (a) Strain profile, (b) displacement profile, (c) SEM and (d) S_{21} magnitude of r_b/r_a = 0.67 resonator in air and liquid.

TABLE III
EXTRACTED PARAMETERS OF SCALED DOWN EPR (R_A = 150 µM AND R_B = 100 µM)

Source		f_n (MHz)	Q	C_m (fF)	(C_m/C_0) %	R_m (kΩ)
Sim.		21.60	-	5.96	0.088%	-
Exp.	air	21.60	1480	5.63	0.083%	0.985
	water	21.54	245	5.49	0.081%	5.5

Despite reducing the device area by 66%, due to a slight increase in Q (245) and resonant frequency, the resulting R_m is less than double (5.5 kΩ). By designing with a more optimal r_b/r_a of 0.8 at this scale of r_a =150 µm, we envisage that R_m can be lowered further to 4.5 kΩ. Table IV compares the performance of two selected EPRs demonstrated in this work with the state-of-the-art summarized. We see that the R_m of the scaled down EPR is comparatively lower than resonators [14] and [25] that have similar surface area. Besides, this EPR is lower compared to devices reported in [13], [18], and [20] that have larger surface area and thus larger comparing area to lower R_m.

TABLE IV
PERFORMANCE COMPARISON WITH THE STATE-OF-THE-ART

Resonance mode [Ref.]	Surface area, A (mm^2)	Transduction method	f_n (MHz)	Q in liquid	R_m in liquid (kΩ)	$R_m \times A$ (kΩ.mm^2)
Lame [9]	0.0025	Capacitive	78	4300	49	0.12
Rotational mode [12]	0.024	Thermal piezoresistive	2.52	537	10.64	0.26
Rotational mode [13]	App. 0.6	Piezoelectric	3.12	150	5.6	3.36
Rotational mode [25]	App. 0.047	Thermal piezoresistive	583	94	316	14.85
Flexural [14]	0.048	Piezoelectric	2.08	100	100	4.8
Button-like [18]	0.125	Piezoelectric	32	362	5.34	0.67
S(4,2) [20]	0.503	Piezoelectric	17.4	490	6.98	3.51
Flexural (0, 1) [28]	0.567	Piezoelectric	0.363	173	79	44.79
EPR (r_b/r_a = 0.8) [This work]	0.157	Piezoelectric	11.53	207	**2.68**	0.42
EPR (r_b/r_a = 0.67) [This work]	0.047	Piezoelectric	21. 54	245	**5.5**	0.26

As mentioned before, for piezoelectric resonators, C_m scales proportionally with area. As such, we have normalized R_m in relation to the device area as a reference figure of merit ($R_m \times A$) for comparison in Table IV. Given that Qs in liquid are expected to be typically low (in the 100s or less), keeping R_m low for resonators targeting liquid-phase is a challenge. As R_m scales with the transduction area of the device, one could reduce R_m with a larger device, but at the cost of reduced mass-sensitivity. As such, the figure of merit based on $R_m \times A$ captures the tradeoff of between size and R_m as well as the contribution of Q in relation to size, which allows a fairer comparison between different resonator topologies and modes for liquid-phase applications reported in the literature. Table IV shows that the scaled down EPR has the lowest value of $R_m \times A$ among all piezoelectric resonators reported to date. Compared to thermal piezoresistive resonators, the piezoelectric EPR has much lower parasitic feedthrough as evident from the large resonant peak to feedthrough ratio with no observable anti-resonance close to the resonant peak of interest. This makes implementing a close-loop self-oscillating circuit practical to realize given these levels of R_m for real-time sensing in liquid-phase applications. Besides, the piezoelectric EPR also does not consume additional power owing to the DC bias current required in thermal piezoresistive resonators.

IV. CONCLUTION

In this paper, we have described a new piezoelectrically transduced micromechanical resonator that we propose for mass sensing in liquid, shaped as an elliptical plate. We have thus referred to this resonator topology as an elliptical plate resonator (EPR). We have described of changing the aspect ratio of the planar dimensions of the device (r_b/r_a ratio) through finite element (FE) simulations and experiments based on fabricated devices, and we show that the simulations and experiments are in good agreement overall. We have shown that EPR can be conveniently clamped at its quasi-nodes without impacting the mode shape significantly, while delivering highly efficient electromechanical coupling compared to other disk-based resonator modes. This in turn lowers the motional resistance (R_m), which is desirable when implementing a close-loop system to track the resonance of the device in real-time for mass-sensing applications. We have shown the advantages and merits of the proposed EPR resonant mode can be preserved as we scale down the size of the device, as desired for mass sensing towards enhancing mass sensitivity by scaling down the proof mass of the resonator. Compared to other resonators in liquid of similar device area, the EPRs in this work have the lowest R_m. The R_m of the proposed EPR is lower than even some other resonators that are notably larger.

REFERENCES

[1] J. Kim, H. J. Kim, E. Cho, H.-J. Shin, J. H. Park, and K. S. Hwang, "Enhancing the sensitivity of a micro-diaphragm resonating sensor by effectively positioning the mass on the membrane," *Sci. Rep.*, vol. 5, no. 1, pp. 17069, Nov. 2015.

[2] S. Marquez, M. Alvarez, J. A. Plaza, L. G. Villanueva, C. Dominguez, and L. M. Lechuga, "Asymmetrically coupled resonators for mass sensing," *Appl. Phys. Lett.*, vol. 111, no. 11, pp. 113101, Sep. 2017.

[3] I.-B. Baek, S. Byun, B. K. Lee, J.-H. Ryu, Y. Kim, Y. S. Yoon, W. I. Jang, S. Lee, and H. Y. Yu, "Attogram mass sensing based on silicon microbeam resonators," *Sci. Rep.*, vol. 7, pp. 46660, Apr. 2017.

[4] T. Y. Kwon, K. Eom, J. H. Park, D. S. Yoon, T. S. Kim, and H. L. Lee, "In situ real-time monitoring of biomolecular interactions based on resonating microcantilevers immersed in a viscous fluid," *Appl. Phys. Lett.*, vol. 90, no. 22, pp. 223903, Jun. 2007.

[5] H. Zhang, M. S. Marma, S. K. Bahl, E. S. Kim, and C. E. Mckenna, "Sequence specific label-free DNA sensing using film-bulk-acoustic-resonators," *IEEE Sens. J.*, vol. 7, no. 12, pp. 1587–1588, Dec. 2007.

[6] M. Khan, A. Khalilian, and S.-W. Kang, "Fast, highly-sensitive, and wide-dynamic-range interdigitated capacitor glucose biosensor using solvatochromic dye-containing sensing membrane," *Sensors*, vol. 16, no. 2, pp. 265, Feb. 2016.

[7] J. Toledo, V. Ruiz-Díez, G. Pfusterschmied, U. Schmid, and J. L. Sánchez-Rojas, "Flow-through sensor based on piezoelectric MEMS resonator for the in-line monitoring of wine fermentation," *Sens. Actuator B Chem.*, vol. 254, pp. 291–298, Jan. 2018.

[8] H. Zhang and E. S. Kim, "Vapor and liquid mass sensing by micromachined acoustic resonators," in *Proc. The 16th annual Int. Conf. on MEMS-03 Kyoto. IEEE,* Kyoto, Japan, 2003, pp. 470-473.

[9] G. Blanco-Gomez and V. Agache, "Experimental study of energy dissipation in high quality factor hollow square plate MEMS resonators for liquid mass sensing," *J Microelectromech. Syst.*, vol. 21, no. 1, pp. 224–234, Feb. 2012.
[10] J. Lee, R. Chunara, W. Shen, K. Payer, K. Babcock, T. P. Burg, and S. R. Manalis, "Suspended microchannel resonators with piezoresistive sensors," *Lab Chip*, vol. 11, no. 4, pp. 645–651, Jan. 2011.
[11] W. Pang, H. Zhao, E. S. Kim, H. Zhang, H. Yu, and X. Hu, "Piezoelectric microelectromechanical resonant sensors for chemical and biological detection," *Lab Chip*, vol. 12, no. 1, pp. 29–44, Jan. 2012.
[12] S. Bhattacharya and S.-S. Li, "A fully differential SOI-MEMS thermal piezoresistive ring oscillator in liquid environment intended for mass sensing," *IEEE Sens. J.*, vol. 19, no. 17, pp. 7261–7268, Sep. 2019.
[13] M. Mahdavi, A. Abbasalipour, and S. Pourkamali, "Thin film piezoelectric-on-silicon elliptical resonators with low liquid phase motional resistances," *IEEE Sens. J.*, vol. 19, no. 1, pp. 113–120, Jan. 2019.
[14] J. Pettine, M. Patrascu, D. M. Karabacak, M. Vandecasteele, V. Petrescu, S. H. Brongersma, M. Crego-Calama, and C. Van Hoof, "Volatile detection system using piezoelectric micromechanical resonators interfaced by an oscillator readout," *Sens. Actuator A Phys.*, vol. 189, pp. 496–503, Jan. 2013.
[15] A. Ali and J. E.-Y. Lee, "Single device on-chip feedthrough cancellation for enhanced electrical characterization of piezoelectric-on-silicon resonators in liquid," *Sens. Actuator A Phys.*, vol. 260, pp. 131–138, Jun. 2017.
[16] A. Ali and J. E.-Y. Lee, "Piezoelectric-on-silicon square wine-glass mode resonator for enhanced electrical characterization in water," *IEEE Trans. Electron. Devices*, vol. 65, no. 5, pp. 1925–1931, May 2018.
[17] A. Ali and J. E.-Y. Lee, "Fully differential piezoelectric button-like mode disk resonator for liquid phase sensing," *IEEE Trans. Ultrason. Ferroelectr. Freq. Control*, vol. 66, no. 3, pp. 600–608, Mar. 2019.
[18] H. Begum, A. Ali, J.E.-Y. Lee, "Mass sensitivity measurements of a novel high Q-factor disk resonator for liquid-phase sensing Applications," in *Proc. 2019 20th Int. Conf. on Solid-State Sensors, Actuators and Microsystems & Eurosensors XXXIII (TRANSDUCERS & EUROSENSORS XXXIII),* Berlin, Germany, 2019, pp. 1886-1889.
[19] A. Rahafrooz and S. Pourkamali, "Rotational mode disk resonators for high-Q operation in liquid," in *Proc. IEEE SENSORS 2010*, HI, USA, 2010, pp. 1071-1074.
[20] H. Mansoorzare, S. Shahraini, A. Todi, N. Azim, D. Khater, S. Rajaraman, and R. Abdolvand, "A microfluidic MEMS-microbalance platform with minimized acoustic radiation in liquid," *IEEE Trans. Ultrason. Ferroelectr. Freq. Control*, vol. 67, no. 6, pp. 1210–1218, Jun. 2020.
[21] M. Baù, M. Ferrari, H. Begum, A. Ali, J. E.-Y. Lee, and V. Ferrari, "Technique and circuit for contactless readout of piezoelectric MEMS resonator sensors," *Sensors*, vol. 20, no. 12, p. 3483, Jun. 2020.
[22] S. Shahraini, M. Shahmohammadi, H. Fatemi, and R. Abdolvand, "Side-supported radial-mode thin-film piezoelectric-on-silicon disk resonators," *IEEE Trans. Ultrason. Ferroelectr. Freq. Control*, vol. 66, no. 4, pp. 727–736, Apr. 2019.
[23] H. Mansoorzare, S. Moradian, R. Abdolvand, "Parylene-coated piezoelectrically-actuated silicon disc resonators for liquid-phase sensing," in *Proc. 2019 20th Int. Conf. on Solid-State Sensors, Actuators and Microsystems & Eurosensors XXXIII (TRANSDUCERS & EUROSENSORS XXXIII),* Berlin, Germany, 2019, pp. 1207-1210.
[24] M. Y. Elsayed and F. Nabki, "Piezoelectric bulk mode disk resonator post-processed for enhanced quality factor performance," *J. Microelectromech. Syst.*, vol. 26, no. 1, pp. 75–83, Feb. 2017.
[25] J. H. Seo and O. Brand, "High Q-factor on-plane-mode resonant microsensor platform for gaseous/liquid environment," *J. Microelectromech. Syst.*, vol. 17, no. 2. pp. 483–493, Apr. 2008.
[26] R. Lu, M.-H. Li, Y. Yang, T. Manzaneque, and S. Gong, "Accurate extraction of large electromechanical coupling in piezoelectric MEMS resonators," *Journal of Microelectromech. Syst.*, vol. 28, no. 2, pp. 209–218, Jan. 2019.
[27] *PiezoMUMPs design handbook*, 1.3 ed., MEMSCAP Inc., Durham, NC, USA, 2013, pp.1 –27.
[28] N. E. Weckman and A. A. Seshia, "Reducing dissipation in piezoelectric flexural microplate resonators in liquid environments," *Sens. Actuator A Phys.*, vol. 267, pp. 464–473, Nov. 2017.

Habiba Begum received the B.Sc. degree in Telecommunication & Electronic Engineering from Hajee Mohammad Danesh Science & Technology University, Bangladesh in 2012 and M.Eng. in Communication & Information Systems from Nanjing University of Aeronautics & Astronautics, China in 2017. Currently, she is pursuing her Ph.D. degree in the department of Electrical Engineering at City University of Hong Kong. Her research interests include designing and characterizing MEMS resonators & oscillators for mass sensing in liquid phase.

Jingui Qian received the BS degree from Wenzhou University, China in 2015 and MS degree from Chonnam National University, Republic of Korea in 2017. Thereafter, he joined the Hong Kong Polytechnic University as Research Assistant. He is currently working toward the Ph.D. degree in the Department of Electrical Engineering, City University of Hong Kong. His research interest includes acoustofluidics cell manipulation, triboelectric nanogenerators, resonator for live cell mass measurement, micro energy harvesting and self-powered sensor/system.

Joshua E.-Y. Lee received the B.A. (Hons) and M. Eng. (Distinction) degrees in 2005, and the Ph.D. degree in 2009, all from the University of Cambridge, U.K. He joined the faculty of the Department of Electronic Engineering, City University of Hong Kong in June 2009, where he is currently an Associate Professor and is affiliated with the State Key Laboratory of Terahertz and Millimeter Waves. He is also the Program Leader for Postgraduate Studies, in which capacity he is responsible for graduate affairs and admissions. In 2017, he was a visiting professor at University Grenoble Alpes in France. His research interests include the design, analysis, and characterization of Micro Electro Mechanical Systems (MEMS) for sensing and frequency control applications. Dr Lee is a Senior Member of the IEEE. He has served on the Technical Program Committees of various conferences including *ISQED*, *IFCS*, and *Transducers*.